

1144
11-24-95
010276

Delay line detectors for the UVCS and SUMER instruments on the SOHO satellite

O. H. W. Siegmund, J. M. Stock, D. R. Marsh, M. A. Gummin, R. Raffanti, J. Hull,
G. A. Gaines, B. Welsh, B. Donakowski, P. Jelinsky, T. Sasseen, and J. L. Tom

Space Sciences Laboratory, University of California, Berkeley, CA 94720

B. Higgins, T. Magoncelli, and J. W. Hamilton

Lockheed Palo Alto Research Laboratory, Palo Alto, CA 94304

S. J. Battel

Battel Engineering, Scottsdale, AZ 85253

A. I. Poland, M. Jhabvala, K. Sizemore, and J. Shannon

NASA Goddard Space Flight Center, Greenbelt, MD 20771

1. INTRODUCTION

Microchannel plate based detectors with cross delay line image readout have been rapidly implemented for the SUMER¹ and UVCS¹ instruments aboard the Solar Orbiting Heliospheric Observatory¹ (SOHO) mission to be launched in July 1995. In October 1993 a fast track program to build and characterize detectors and detector control electronics was initiated. We present the detector system design for the SOHO UVCS and SUMER detector programs, and results from the detector test program. Two deliverable detectors have been built at this point, a demonstration model for UVCS, and the flight Ly α detector for UVCS, both of which are to be delivered in the next few weeks. Test results have also been obtained with one other demonstration detector system.

The detector format is 26mm x 9mm, with 1024 x 360 digitized pixels, using a low resistance Z stack of microchannel plates (MCP's) and a multilayer cross delay line anode (XDL). This configuration provides gains of $\approx 2 \times 10^7$ with good pulse height distributions ($< 50\%$ FWHM) under uniform flood illumination, and background levels typical for this configuration (≈ 0.6 event $\text{cm}^{-2} \text{sec}^{-1}$). Local counting rates up to ≈ 400 events/pixel/sec have been achieved with no degradation of the MCP gain. The detector and event encoding electronics achieves $\approx 25\mu\text{m}$ FWHM with good linearity (± 1 pixel) and is stable to high global counting rates ($> 4 \times 10^5$ events sec^{-1}). Flat field images are dominated by MCP fixed pattern noise and are stable, but the MCP multifiber modulation usually expected is uncharacteristically absent. The detector and electronics have also successfully passed both thermal vacuum and vibration tests.

2. MISSION AND INSTRUMENT REQUIREMENTS

The UVCS and SUMER experiments are two of 12 experiments aboard the SOHO mission platform. Both are spectroscopy experiments, but have different roles to play in the SOHO mission. The UVCS spectrograph will examine the solar corona out to ≈ 10 solar radii in the wavelength range 500 - 1300Å. Determination of spectral line profiles and intensities will allow investigations of coronal heating, and solar wind acceleration and composition. The UVCS optical system employs off axis parabolic mirrors and toroidal reflection gratings. UVCS has two separate channels with XDL detectors, one optimized for the Lyman α region (1148Å - 1283Å), and the other for the O VI region (932 - 1068Å), which also accomodates Si XII (499Å & 521Å) in second order. The SUMER spectrograph will examine regions of the solar atmosphere in the wavelength range 500 - 1600Å. Primary goals are the study of flows, turbulent motions, and temperatures and

densities of the upper solar atmosphere. The SUMER spectrograph utilizes one primary detector and one secondary detector for safety. The primary, on axis, detector is at the focus of a two off-axis parabolic mirror, plane mirror, spherical concave grating optical system. The secondary detector is displaced by $\approx 7\text{cm}$ from the primary. The spectrograph plane mirror is movable, allowing the spectral lines to be scanned across the primary detector, or selection of the secondary detector.

The spectral and spatial resolution needed for these experiments requires a focal plane detector that is 26mm in length and 9 mm high with a 1024 x 360 pixel format. Other basic requirements for the SOHO UVCS and SUMER detectors derived from the science goals and the instrument design are: a resolution of $\approx 25\mu\text{m}$ in X (dispersion direction) and in Y (cross-dispersion direction), quantum detection efficiency (QDE) $>7\%$ @ 584Å and $>20\%$ @ 1066Å, and counting rate capacity of $>4 \times 10^5$ events sec^{-1} (SUMER).

3. DETECTOR SYSTEM

3.1 Detector design

The basic detector design for both the SOHO UVCS and SUMER experiments is displayed in Fig. 1. A brazed metal-ceramic detector body, into which the MCP's are mounted, provides ruggedness and low weight. The detector has a circumferential spring clamping arrangement for the MCP stack that has proven to be successful on a number of earlier flights². The scheme uses three 80:1 channel length/diameter (l/d) MCP's in a "Z" stack. MCP's were obtained from two vendors, Philips and Galileo, to assure a supply of "flight" MCP's. The Galileo MCP's have 10 μm pores (12.5 μm spacing) with 12° bias angle, on a 36mm circular borderless format and resistance of $\approx 30\text{M}\Omega$ per MCP. The Philips MCP's have 12.5 μm pores (15 μm spacing) with 13° bias angle, on a 36mm circular borderless format and resistance of $\approx 20\text{M}\Omega$ per MCP. The field of view (26 x 9mm) is defined by an aperture mask placed in contact with the top MCP (Fig. 2). The brazed detector body is attached to a support plate (Fig. 2) that clamps the readout anode in place on the vacuum flange with a $\approx 7\text{mm}$ MCP to anode gap. The cross delay line (XDL)³ anode has a "charge collection" area (33mm x 15mm) with external "delay lines", and is constructed on an alumina ceramic substrate. The detector flange is made of titanium for low weight, and contains both signal and high voltage feedthroughs (Fig. 2). There is a pumping port on the flange to allow purge and vacuum lines to be attached to the backside for various testing scenarios. The amplifier electronics box and the high voltage power supply are both mounted to the detector flange. Not shown in the figure are the vacuum housing which covers the detectors, the MgF₂ window used for the UVCS Ly α detector, and the meshes for attenuation of Ly α on both SUMER detectors. There is also a thermal ion rejection mesh covering the entrance aperture for the UVCS O-VI detector, and electrostatic thermal ion deflectors for both SUMER detectors.

Operationally, the detector is similar to other devices that we have implemented in various space programs. An opaque KBr photocathode is deposited on the MCP Z stack, and incoming photons interact with the photocathode, resulting in photoelectron emission^{4,5}. The photoelectrons impact the walls of MCP pores causing a charge avalanche, giving an overall charge multiplication of $\approx 2 \times 10^7$. This charge cloud is drifted from the MCP output to the delay line anode (Fig 3). The charge is divided $\approx 50\%/50\%$ between the XDL charge collection fingers in the X and Y axes which are connected to X and Y external serpentine delay lines (Fig 3). X and Y photon event centroid positions are deduced from the signal arrival time differences at the two ends of each delay line. Image encoding electronics provides the necessary processing for event position determination, and digitizes the X and Y event positions prior to data histogramming and telemetry to the ground.

3.2 Cross delay line anode

The XDL image readout has been selected for SOHO UVCS and SUMER on the basis that it can achieve the required resolution and high counting rate performance. This anode design is both compact and robust allowing considerable flexibility in design to match specific size constraints.

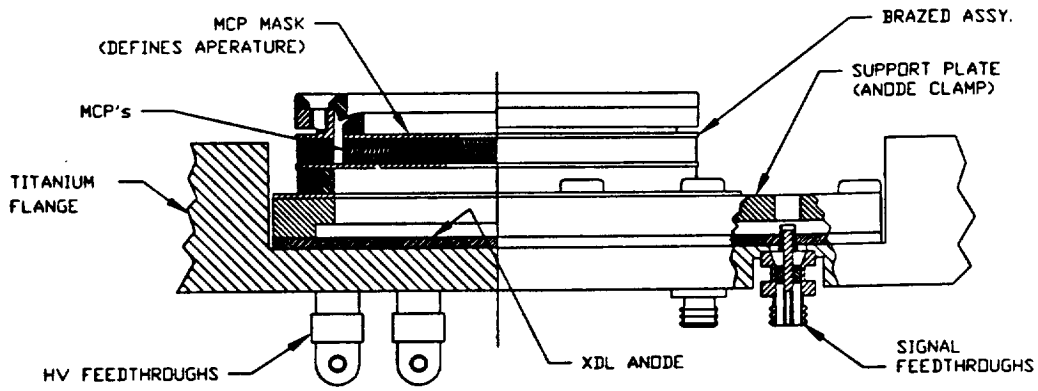


Figure 1. Drawing of the SOHO SUMER/UVCS detector subassembly design.

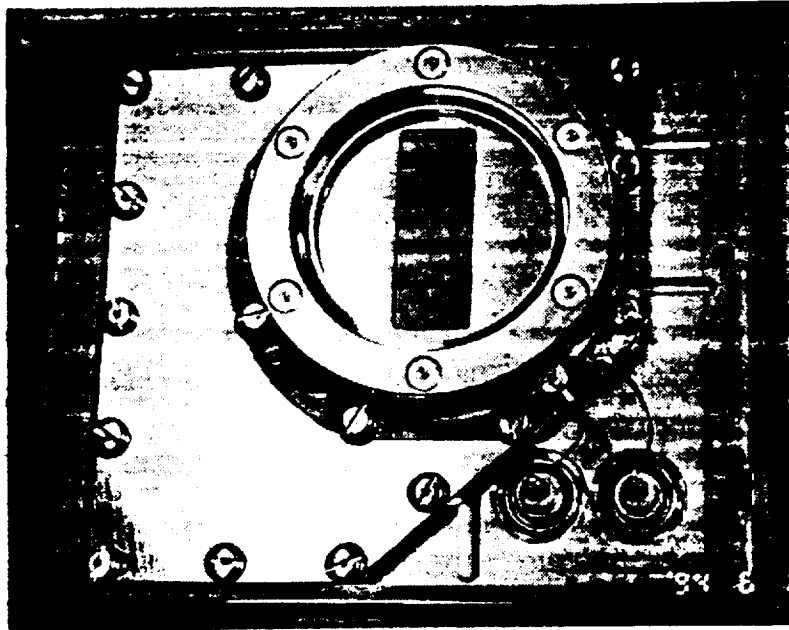


Figure 2. Photograph of the Flight UVCS Ly α detector subassembly showing the rectangular field of view, high voltage feedthroughs and mounting flange.

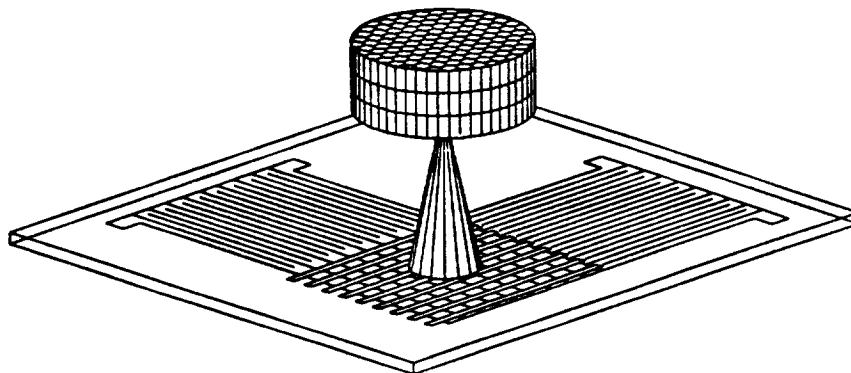


Figure 3. Schematic of the operational configuration of the SOHO XDL detectors, showing the MCP stack and electron cloud impinging on the XDL anode.

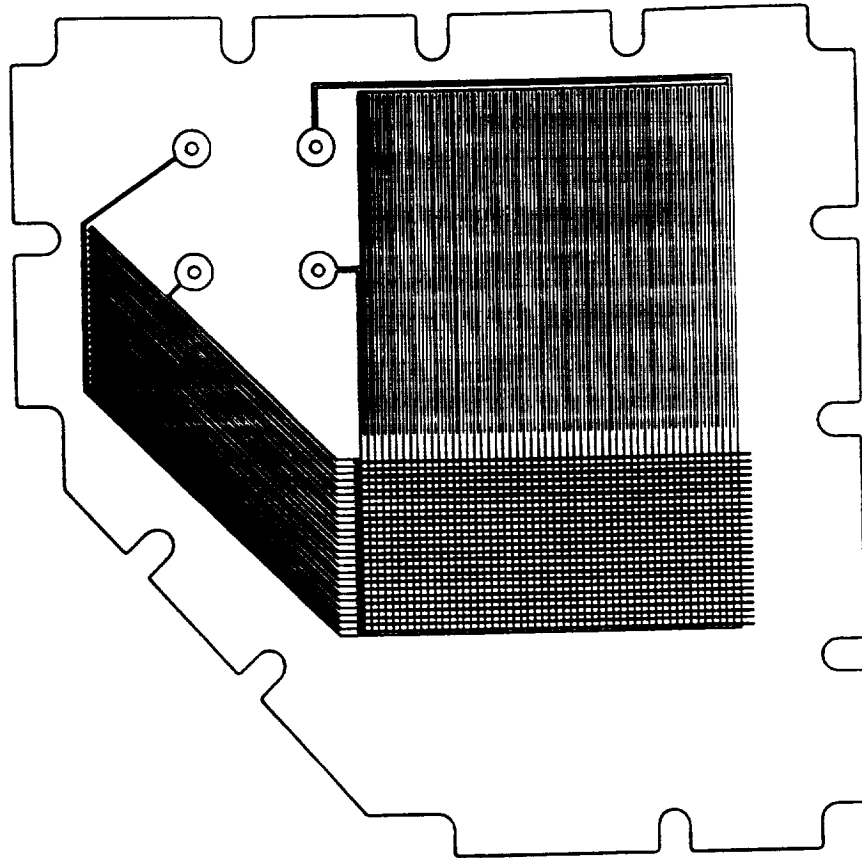


Figure 4. Schematic of the SOHO XDL anode pattern, illustrating the X and Y external delay lines, and the central area composed of crossed X and Y strips with an insulated set of ground plane fingers interposed.

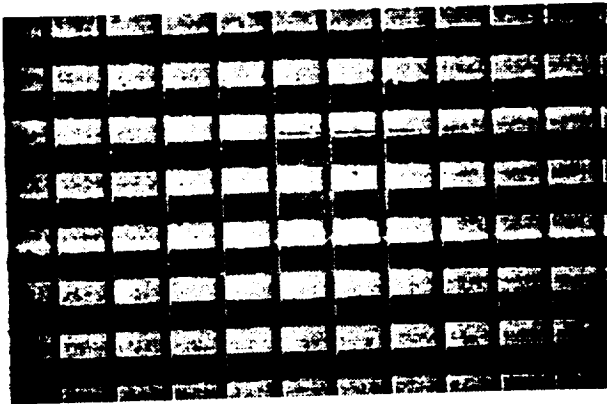


Figure 5. Photograph of central area of the SOHO XDL anode showing the X and Y charge collection fingers.

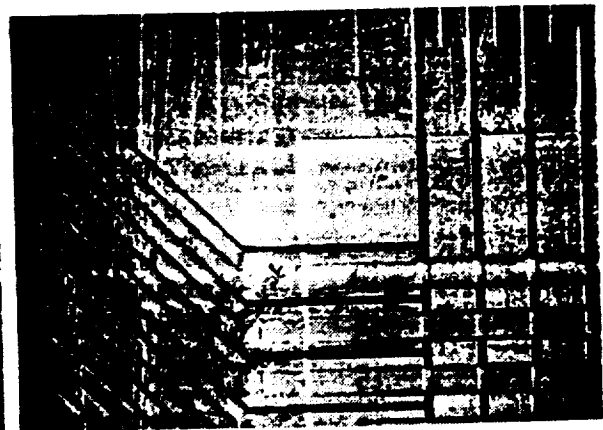


Figure 6. Photograph of a corner of the SOHO XDL anode showing the X and Y fingers and portions of the X and Y delay lines.

Delay lines of this type are produced by a multi-step process to cut the anode pattern into conductor and insulator layers deposited on a low loss microwave substrate. The MCP charge pulse (≈ 3 to 5 ns width) is detected on, and divided between, two sets of conductive fingers. The SOHO XDL scheme has two orthogonal sets of fingers (Fig. 4) in a charge collection area of 33mm x 15mm. The fingers in both axes have a 0.6mm period, with the X fingers beneath the Y fingers. The Y fingers are ≈ 0.5 the width of the X fingers to allow 50% of the charge to fall on each set (Fig. 5). The two sets are separated by a grounded set of fingers and two thin, low ϵ layers (polyimide) which have the same geometry as the upper Y finger set. The fingers in each axis are connected to "external" serpentine delay lines cut into a Cu layer on an alumina substrate ($\epsilon \approx 10$, 250 μ m thick). A ground plane is sandwiched between this "upper" ceramic, and a thicker (1mm) alumina backing used for support. The XDL fingers in each axis are each connected along the external delay lines (Fig. 6) so that the charge is propagated along the delay line from the finger attachment points. The pulse arrival time at each end of each delay line is thus a linear function of the X, or Y, position of the original event. The photon event centroid is encoded through determination of the difference in arrival times of the event signal at the two ends of the serpentine (distributed R-C) delay line (Fig.4). The high permittivity (ϵ) value of the substrate reduces the pulse propagation speed, thus increasing the total anode delay per unit length. Thick Cu and low dielectric loss coefficient minimize the pulse attenuation and dispersion as it travels across the anode. End to end delay times are ≈ 30 ns ($V \approx 10^6$ m sec $^{-1}$) in X and 15ns in Y. The delay line of the Y axis (Fig.4, 6) was "slanted" at a $\approx 45^\circ$ angle to accommodate the space constraints of the flange design for the SOHO application.

3.3 Imaging electronics

The delay line encoding electronics are fairly straightforward, consisting of a fast amplifier and a constant fraction discriminator (CFD) for each end of each delay line, followed by time to amplitude (TAC), and analog to digital converters (ADC) (Fig. 7) constituting a time to digital converter (TDC). Both fast amplifiers for each axis are on single boards, two of these are required for each detector and are installed in a single box bolted directly to the detector flange. These amplifiers contain low pass frequency filters to increase the signal to noise ratio. The amplifier design also includes charge sensitive amplifiers with bipolar shaping on each axis, so that the pulse amplitude of the signals can be measured. These are digitized and folded into the telemetry to give a measure of the gain performance of the microchannel plates throughout the mission. Another feature of the system is that an artificial pulse (stimulation pulse) is injected into each delay line at a rate of ≈ 40 sec $^{-1}$, resulting in a spot image effectively at the center of the detector aperture. This stimulation pulse is also continuously ramped up and down in amplitude. The data obtained from this feature allows amplitude walk, and position shifts due to potential electronics changes in orbit to be evaluated and possibly corrected.

"Start" and "stop" amplifier signals from each delay line axis are harnessed via coaxial cables to the TDC box. Constant fraction discriminators are used for each of the four signals to provide fast logic output pulses that are sent to a time to amplitude converter circuit for each axis. The time to amplitude converter output is $\approx 0.5\mu$ s wide with an amplitude proportional to the time lag between the start and stop pulses. A 12 bit, 1 MHz analog to digital converter is then used to digitize the two pulse amplitudes, giving a direct measure of the original photon centroid position. The full range of the TDC is adjustable so that the area of choice on the anode may be selected. Although the ADC digitized positions are of 12 bit accuracy, they are passed on to the instrument electronics in 10 bit X by 9 bit Y format to match the original specifications for the system. Differential nonlinearity due to $\pm 50\%$ variations in the width of the least significant bit in the ADC is reduced by employing³ a "dither" to the X axis ADC input and then digitally subtracting it at the ADC output. This is conveniently performed by a programmable gate array (Actel) on the TDC, providing an averaging of the ADC DNL over a number of channels. The differential non-linearity is substantially reduced

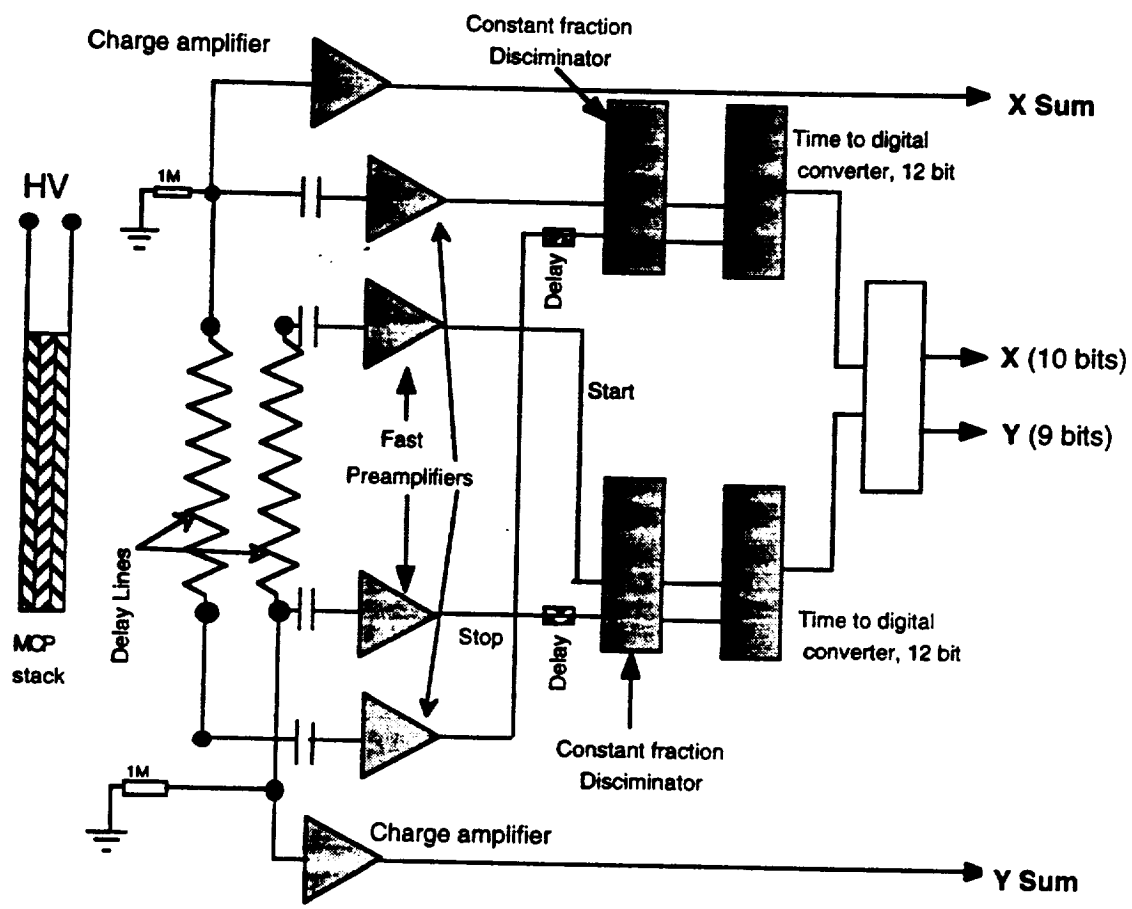


Figure 7. Schematic of the SOHO UVCS/SUMER position encoding electronics scheme for the XDL detectors

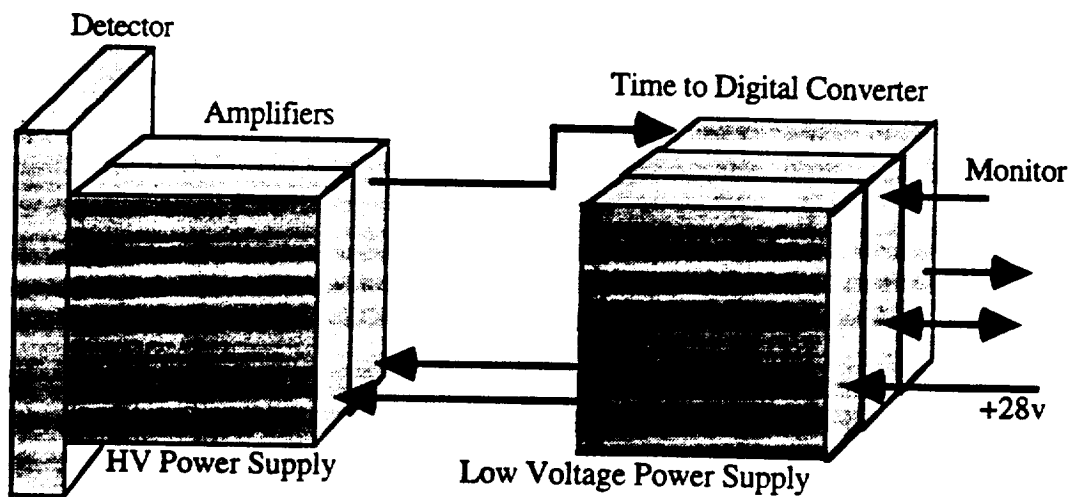


Figure 8. Block diagram of the SOHO UVCS/SUMER XDL electronics boxes used for detector system commands, housekeeping, power and data processing.

providing a better pixel to pixel uniformity for the spectral (X) direction of the detectors. There are two boards in the flight TDC box, one for each axis.

The position resolution of the XDL detector electronics system is determined⁶ by the event timing error. This includes a number of factors; signal attenuation and dispersion, preamplifier noise, discriminator walk and jitter, TAC noise, and ADC errors. The limiting electronic resolution for the SOHO XDL electronics is $\approx 15\mu\text{m}$ FWHM as determined by end to end testing with the stimulation pulser. The performance of the electronics has also been examined in thermal tests and show that, after solving initial problems with a low temperature coefficient capacitor in the TDC, the image drift is ≈ 1 pixel/ 10°C . This is acceptable since the thermal conditions in orbit are expected to be quite stable. Performance as a function of counting rate has also shown that the image position stability is better than 1 pixel up to >500 KHz, with only a 25% degradation of position resolution at 600 KHz.

3.4 Command and control electronics, and power supplies

The command and control functions for the SOHO XDL detectors are provided by the monitor box. This interprets serial commands from the instrument control system, and outputs within the same serial stream all engineering housekeeping data. Specific types of command functions include high voltage control, signal threshold level adjustments, and stimulation pulser control. Housekeeping data includes power supply voltage monitors, multiple pulse height data, fast event counters, temperatures of all sub-assemblies, and both monitored and digitally echoed values for all signal amplitude threshold settings and controlled voltages, such as thresholds and high voltage settings. The low voltage power supply uses pulse width modulation to provide multiple regulated low voltage outputs from the input $+28\text{V}$. The power is directed to the amplifier, TDC, monitor, and high voltage power supply box, each with isolated returns (Fig. 8). The high voltage power supply produces up to -5.5KV , programmable with 8 bits resolution starting at -2.0KV , and a fixed -900V potential for the MCP output to anode. Both voltage and current monitors are routed to the monitor box. Electrical ground support equipment (GSE), primarily consisting of a SUN workstation and an interface box is used to command and acquire all instrument data. In the instruments the TDC digital position data are directly piped via a simple parallel interface to the instrument data processors. For ground testing we have employed an electrical ground support system consisting of an interface box, and a digital signal processor card in the S-bus slot of the Sun Sparcstation. Menu driven GSE software displays all housekeeping data including a running histogram of the acquired PHA data, and a real time detector X-Y image display.

4. Detector System Performance

4.1 Microchannel plates

An opaque KBr photocathode is applied to the front of the MCP's in the SOHO XDL detectors to improve the quantum detection efficiency (QDE) at the wavelengths of interest. The photocathode fabrication and evaluation process is defined by our previous detailed studies of photocathode materials^{4,5} and applications to other missions. For UVCS the photocathode covers the entire detector field of view, but only the central 50% of the SUMER detectors is coated with KBr. Two SOHO detectors (a UVCS demonstration model and the UVCS Ly α flight #1 detector) have already been coated with KBr and are currently in the measurement phase. We expect to achieve $>30\%$ QDE for 584\AA , and $>25\%$ 1066\AA based on measurements of other KBr photocathodes. Since the SOHO detectors are open face and N_2 purged, we rely on our lifetest data⁷ combined with experience in handling these photocathode materials in previous missions to ensure preservation of the photocathode QDE.

Several MCP stacks have been tested in the SOHO XDL detectors. The flight UVCS Ly α detector results in Figures 9 and 10 show that good gain and pulse height results have been obtained, with gains $>2 \times 10^7$ and pulse height spectra with gaussian shape and widths $<50\%$ FWHM under full flood illumination with a Hg vapor lamp (2537\AA). The overall background rate is

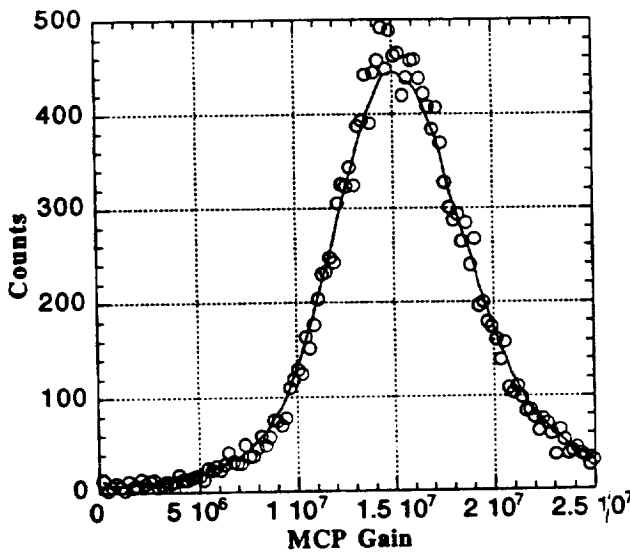


Figure 9. Pulse height spectrum for UVCS Flight #1 detector with Philips MCP's.

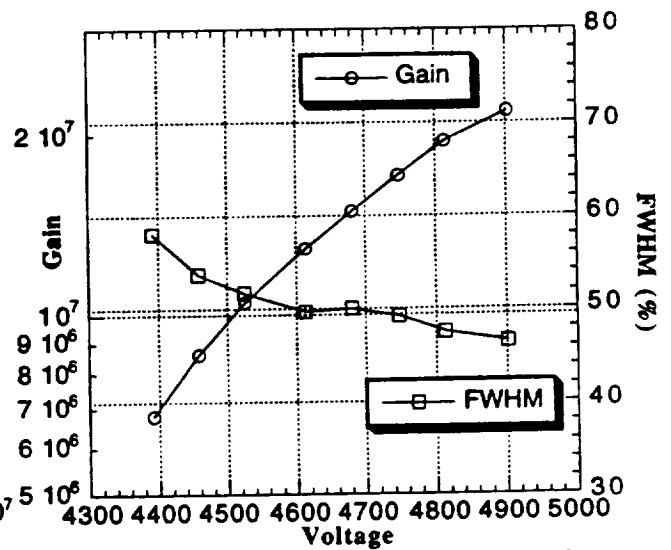


Figure 10. Gain and pulse height vs. voltage for UVCS Flight #1 detector & Philips MCP's.

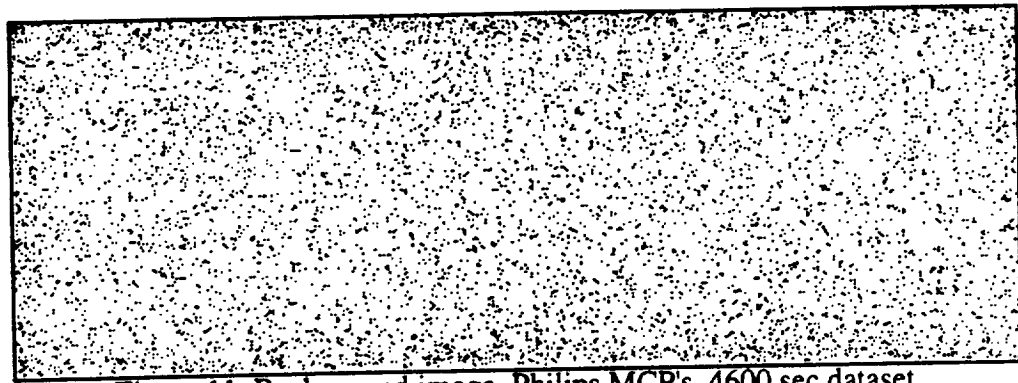


Figure 11. Background image, Philips MCP's, 4600 sec dataset.
Rate ≈ 0.6 events/cm²/sec, gain = 1.5×10^7 .

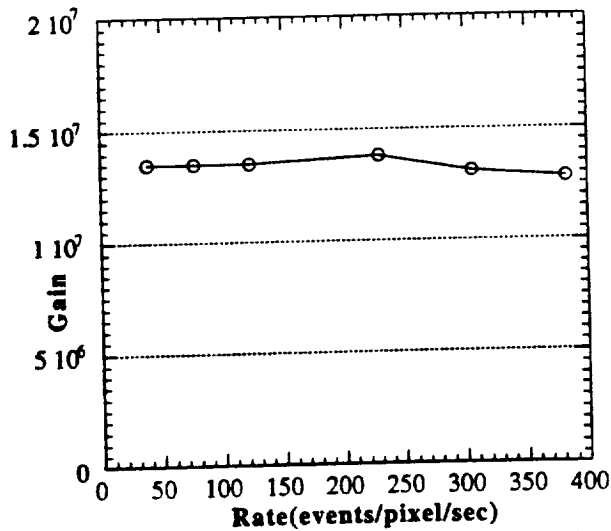


Figure 12. Gain vs. local ($10\mu\text{m}$ spot) counting rate, Philips MCP stack ($R_{\text{mcp}} = 20\text{M}\Omega$).

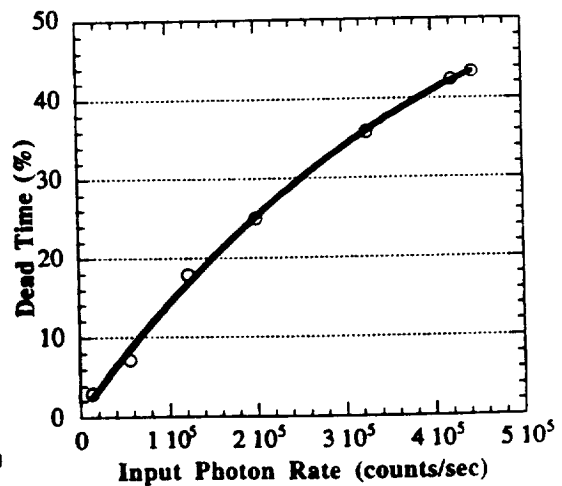


Figure 13. Readout electronics dead time as a function of input counting rate.

as expected for intrinsic β decay MCP noise^{8,9} (Fig. 11) for ^{40}K in the Philips glass, with a rate of ≈ 0.6 events sec^{-1} uniformly distributed across the field of view. Using a pinhole mask with $10\mu\text{m}$ pinholes the effect of high local counting rates on the MCP gain was also investigated. The local event rate capacity is controlled by the resistivity of the MCP stack. To maintain a compromise so that the power dissipation of the MCP's is kept low, and to limit the power required for the high voltage supply, resistance values in the range $250\text{M}\Omega/\text{cm}^2$ were selected for the SOHO XDL MCP's. Results (Fig. 12) show that for these MCP's the gain remains stable up to ≈ 400 events $\text{pixel}^{-1} \text{sec}^{-1}$, which exceeds the SOHO XDL mission application requirements. The global counting rate is controlled by the electronics processing speed. Detector tests (Fig. 13) show that rates of $>4.5 \times 10^5 \text{sec}^{-1}$ can be achieved with $\approx 45\%$ dead time ($6 \times 10^5 \text{sec}^{-1}$ has been achieved with little effect on imaging performance) for the position encoding stream, mainly limited by the ADC reset time ($\approx 1.3\mu\text{s}$).

4.2 Imaging performance

The imaging resolution and linearity of the SOHO XDL detectors is measured using images of a set of $10\mu\text{m}$ diameter test-mask pinholes. A typical image of such a test mask is shown in Fig. 14. Cross sectional histograms such as those displayed in Figures 15 and 16 allow the X and Y image centroids and widths (FWHM) to be determined for each pinhole image. The resolution of the detector system is of the order $25\mu\text{m}$ FWHM (Fig. 16) in both axes, and above gains of $\approx 1 \times 10^7$ is not signal to noise dependent. No corrections to the data have been made either, since when the amplitude walk adjustments have been made to the CFD there is little observable position drift with amplitude. Image non-linearities are measured by comparison of the measured pinhole image positions to the expected pinhole mask array positions. Position deviations (Fig.17) are typically less than $20\mu\text{m}$, which is comparable with the mask pinhole fabrication position error ($\approx 10\mu\text{m}$) plus the expected $\pm 10\mu\text{m}$ jitter due to MCP pore position uncertainty with respect to the pinhole locations. Neither the resolution or the image linearity are significantly affected by changes of the MCP to anode acceleration field, or by altering the MCP gain.

A contrast enhanced image (1024×360) of a flat field exposure for the SOHO UVCS flight #1 detector after the KBr photocathode was deposited, is shown in Fig. 18. Although the Kr lamp was diffused by using a LiF diffuser, the input illumination global uniformity was not independently checked, and may not be quite flat. Overall, very little flat field modulation is seen, and all the observed variation is due to MCP effects. No anode related modulations were seen. One unusual feature is that modulation due to the MCP multifiber structure is not very evident. Typical MCP modulation at the multifiber boundaries is of the order $10\%-15\%$ ¹⁰. Earlier data in another SOHO detector with a set of Galileo MCP's displayed this characteristic image modulation. However, only slight indications of a multifiber image can be seen in the Fig. 18 image when displayed on the computer screen. At least one other MCP set from this batch of Philips MCP's has undergone the same testing in the UVCS demonstration detector, and it too displays very little MCP multifiber modulation. It is thought that this performance is a direct result of the fabrication process for the entire boule of material from which these MCP's came. Earlier results have linked the MCP multifiber modulation to physical distortions of the MCP pores at the boundaries of the multifibers¹⁰. A single pixel histogram in X, and a histogram of the entire histogram in X are shown in Fig. 19 a,b. These show that there is a $\approx 20\%$ variation in the image intensity from one side to the other. Whether this is due to variations in the cathode QDE or the illumination is under investigation currently. One fairly large dead spot is clearly visible in the flat field image shown in Fig. 18, which is due to an MCP fabrication defect. The differential variations on a pixel to pixel scale, however, show no periodic modulations, demonstrating the efficiency of the ADC "dithering" technique to remove ADC bin to bin differential nonlinearity. A histogram of the statistics of the intensity map of a $3\text{mm} \times 3\text{mm}$ area of the image (to avoid the global intensity variation) is shown in Fig. 20. This data matches well with the expected statistical variations for a flat field of this level. Many of the flat field features can cause errors in actual observations, even when the flat field

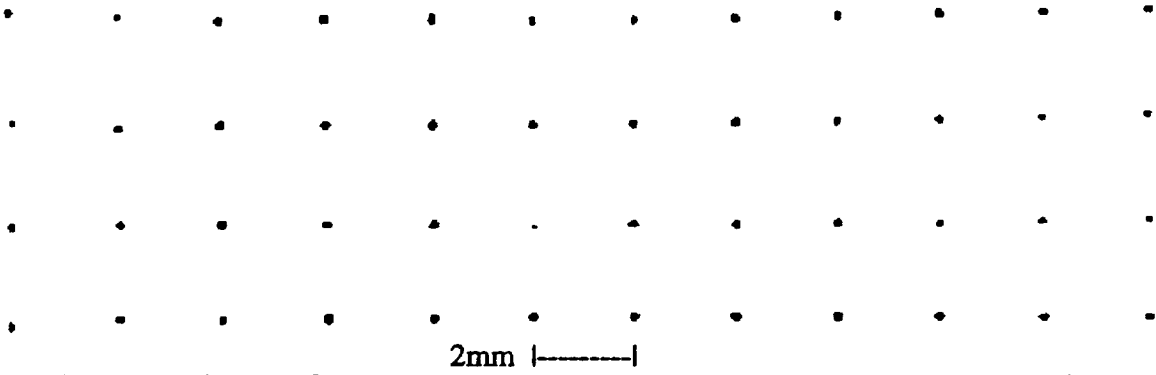


Figure 14. Image of a 2mm x 2mm spaced array of 10 μ m diameter pinholes using the SOHO XDL detector. Gain = 2×10^7 , 2537 \AA illumination.

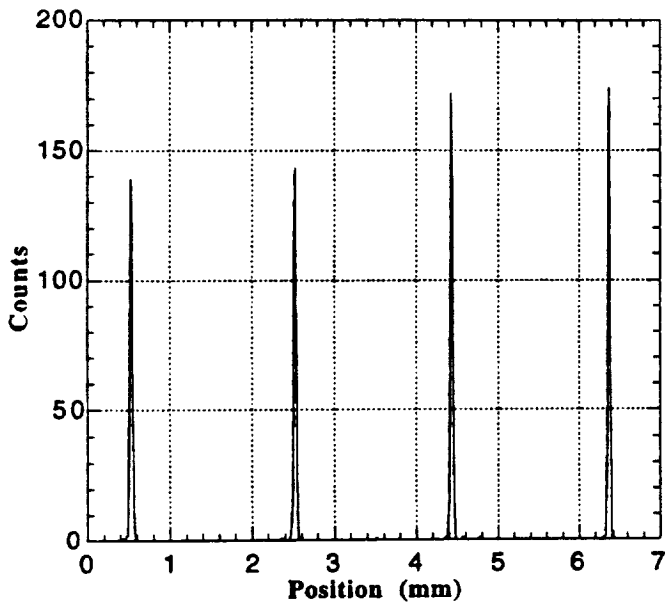


Figure 15. X direction histogram of 4 pinhole images shown in Fig. 14.

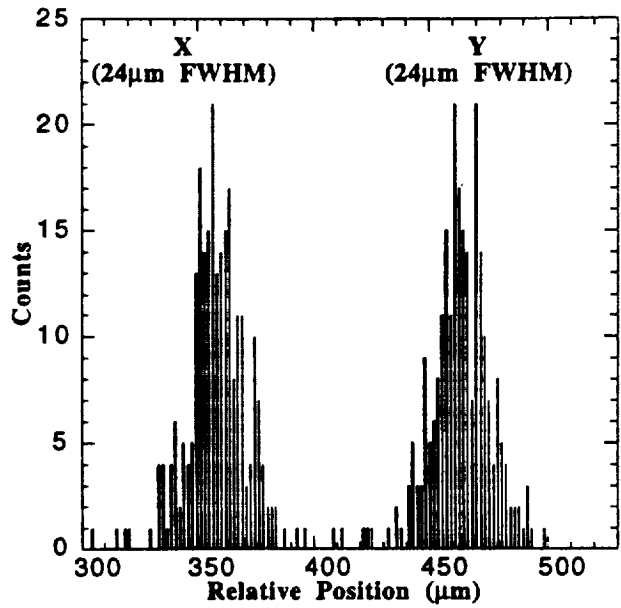


Figure 16. X & Y direction histograms of one of the pinhole images shown in Fig. 14.

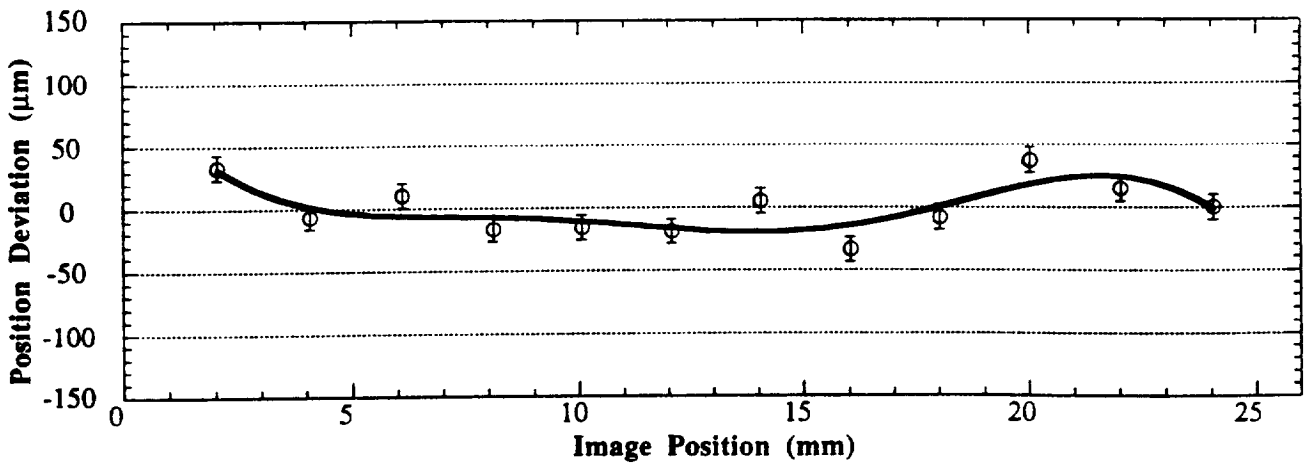


Figure 17. Position nonlinearity, derived from pinhole image position deviations from the expected positions, for one row of pinhole images shown in Fig. 14.

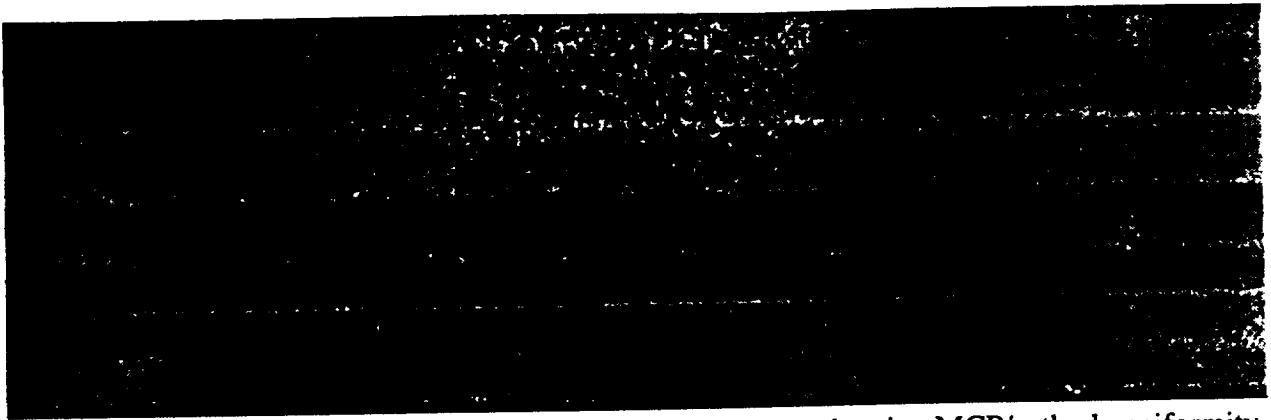


Figure 18. Flat field image of the SOHO UVCS Ly α detector showing MCP/cathode uniformity & a MCP dead spot. Kr (1237\AA) source, gain 1.7×10^7 , 10^8 events total at 100k events/sec.

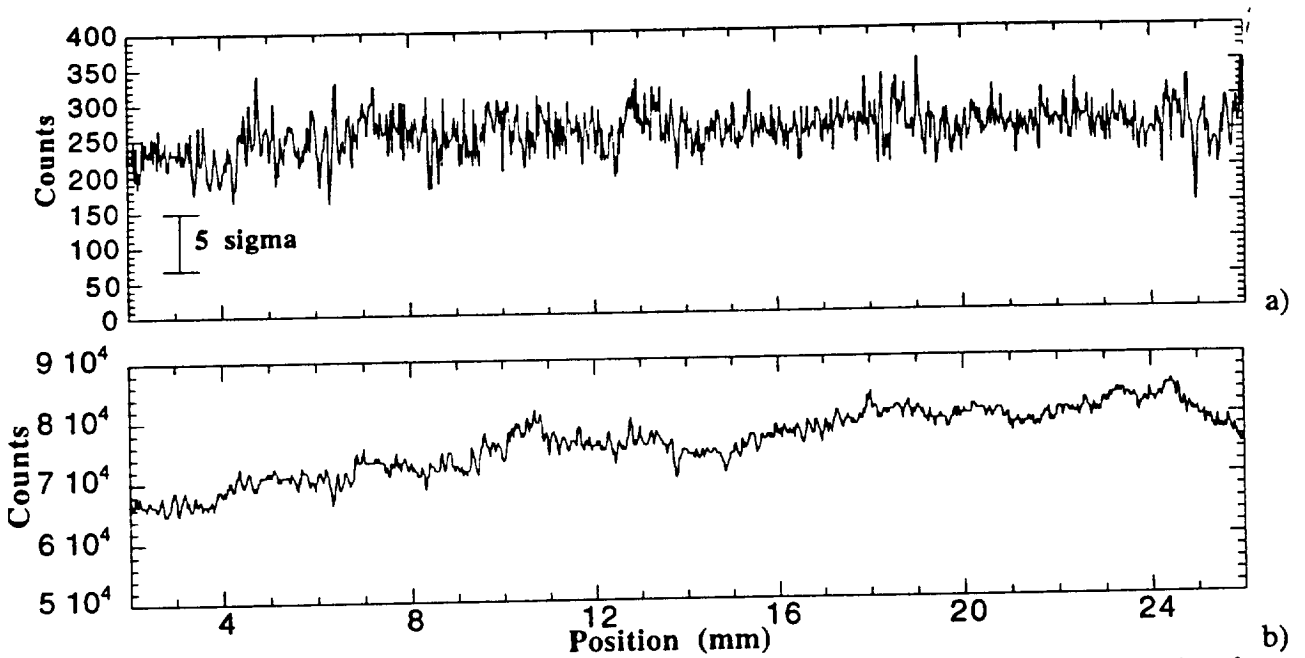


Figure 19 a,b. X histograms for a single pixel (a), and the entire image (b) in Fig. 18. showing the flat field integral and differential non-uniformities.

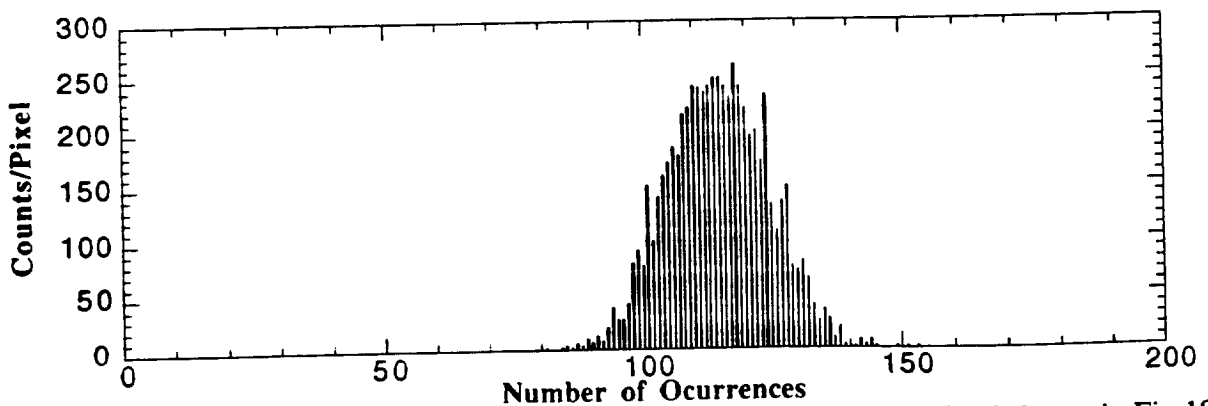


Figure 20. Statistical analysis of the intensity uniformity of a zone of the flat field shown in Fig.18.

modulations are divided out. Progressively shifting the spectra during some observations is planned, to accomplish a "dithering" effect to remove the local fixed pattern noise with image deconvolution techniques¹¹.

5. Acknowledgments

Many grateful thanks are extended to the many unmentioned people who contributed to this effort at U.C. Berkeley, Lockheed, and the Goddard Space Flight Center. We also thank Philips and Galileo for their response to the challenge on the MCP fabrication, and Kyocera for fabrication of the anode substrates.

This work was supported by Fairchild contract #SC-00858, and NASA grant NAG5-2304.

6. References

1. The SOHO mission, ESA SP-1104, (1988)
2. Siegmund, O.H.W. M.A. Gummin, J. Stock and D. Marsh, ESA symposium on detectors, ESA SP-356, 89-96, December 1992.
3. Siegmund, O.H.W. M.A. Gummin, J. Stock, D. Marsh, R. Raffanti, and J. Hull, *Proc. SPIE*, **2006**, 176-187 (1993).
4. Siegmund, O.H.W. E. Everman, J. Vallergera, J. Sokolowski, and M. Lampton, *Applied Optics*, **26(17)**, 3607 - 3614 (1987).
5. Siegmund, O.H.W. and G. Gaines, *Proc. SPIE*, **1344**, 217-227 (1990).
6. Siegmund, O.H.W., Lampton, M., and Raffanti, R., *Proc. SPIE*, **1159**, 476 (1989).
7. Marsh, D. O.H.W. Siegmund, and J. Stock, *Proc. SPIE*, **2006**, 51-81 (1993).
8. Siegmund, O.H.W., Vallergera, J., and Wargelin, B., *IEEE Trans. Nucl. Sci.*, **NS-35**, 524 (1988).
9. Fraser, G.W., Pearson, J.F., and Lees, J.E., *Nucl. Instrum. & Meth.*, **A254**, 447 (1987).
10. Vallergera, J.V., Siegmund, O.H.W., Vedder, P.W., Gibson, J., *Nucl. Instrum. & Meth.* **A310**, 317-322 (1991).
11. Sahnou, D. J., C. W. Bowers, O. H. W. Siegmund, J. Stock, and M. A. Gummin, *Proc. SPIE*, **1945**, April, (1993).